

# Dirac points and Weyl phase in a honeycomb altermagnet

Meng-Han Zhang , Xuan Guo , and Dao-Xin Yao\*

Guangdong Provincial Key Laboratory of Magnetoelectric Physics and Devices, State Key Laboratory of Optoelectronic Materials and Technologies, Center for Neutron Science and Technology, School of Physics, Sun Yat-Sen University, Guangzhou, 510275, China

\*yaodaox@mail.sysu.edu.cn

## ABSTRACT

We present a graphene derivative displaying novel topological phenomena without the spin-orbit coupling (SOC) in a collinear altermagnet. By investigating the retarded and advanced Green's functions, we calculate the spectral density and amplitude of wave function whose exact solutions are analytically obtained. The altermagnetism breaks the intrinsic time-reversal symmetry, guaranteeing the formation of pairs of Weyl points associated with the internal spin structure chiralities. We demonstrate the evolution of Dirac and Weyl crossings, in which spontaneous Hall effect is controlled by the chiral edge modes. Topological phase transitions are characterized by the high Chern numbers preserving the non-intersecting flows of Wannier centers over occupied bands. We illustrate possible experiments to realize topologically altermagnetic responses according to the bulk-boundary correspondence.

Despite the zero net magnetization, altermagnets can exhibit non-trivial Berry phase since their specific staggered spin configuration breaks time-reversal symmetry. Their classification on account of the resulting magnetic order from tetragonal and hexagonal families hints at a hybrid pairing mechanism involving both spin-singlet and spin-triplet components<sup>1,2</sup>. Associated with the formation of a spontaneous internal magnetic field, the altermagnetism has potential for spontaneous Hall effect generated by the finite Berry curvature<sup>3-6</sup>. It has been shown that an antiferromagnetic honeycomb monolayer with parity-time ( $PT$ ) symmetry<sup>7</sup> can be categorized into  $d_{x^2-y^2}$  or  $i$ -wave altermagnet rather than the majority of  $d_{xy}$  and  $g$ -wave symmetries<sup>8-11</sup>. Splitting the energy bands with  $k$ -dependent spin polarization, the topological nature of the altermagnet can interact with Cooper pairs and alter the symmetry of the superconducting order parameter<sup>12,13</sup>.

We assume a graphene derivative in wallpaper group  $p6m$  with additional symmetry constraints imposed by the six-fold rotation<sup>14,15</sup>. The altermagnetic order combines spin space rotation with a mirror symmetry for sublattices  $A, B, C, D$  in the presence of staggered magnetization<sup>16-18</sup>. Grounded in spinless electrons on a tight binding model, bond dimerization introduces an alternating pattern of hopping strengths<sup>19</sup>. When spin-orbit coupling (SOC) is neglected, tilted Dirac and Weyl crossings are the consequences of the interplay between the spin splitting and the buckling of honeycomb lattice<sup>20-22</sup>. We calculate the Green's function under the Matsubara representation for the spectrum of nanoribbons, which facilitate the study of the insulating or semiconducting behaviors<sup>23,24</sup>. The zigzag ribbon presents van Hove singularities (vHSs) in the density of states (DOS) that is absent in the armchair case<sup>25</sup>. Quantized transport property is a manifestation of its underlying topology, indicating the presence of gapless chiral edge states and dissipationless spin currents<sup>26</sup>. The gapped cross-

ings can enhance photocatalytic activity improving carrier concentration at the interface, which provide a fertile ground to manipulate the valley polarization in the band structure and realize the valley-selective optical transitions<sup>27</sup>.

## Altermagnetic wallpaper groups

We present a monolayer honeycomb lattice breaking the time-reversal symmetry ( $-i\sigma_y K$ ) in altermagnetic wallpaper group  $p6m$ <sup>16</sup>. The magnetic moments on adjacent lattice sites are aligned in opposite directions lifting the degeneracy of energy bands<sup>28</sup>. The antiparallel orientation of magnetic moments interacts differently with the up and down spin states akin to the Zeeman effect, albeit in the absence of external magnetic fields<sup>29,30</sup>. Preserving macroscopic net zero magnetization, we study the splitting of energy bands that contribute to the formation of linear crossings. Similar to the topological protection of Weyl points, the crossings are protected by the combined action of time-reversal symmetry and mirror symmetry<sup>31,32</sup>. The Weyl crossings are isolated in momentum space evolving along the high-symmetry directions<sup>21,22</sup>. The symmetry operators with spin and lattice indices allow for the exploration of topological phenomena in magnetic materials<sup>33-37</sup>.

We respectively flip the spin on mirror and rotational symmetries related with two opposite-spin mapped to each other through the  $M_x$  mirror<sup>38,39</sup>. The mirror symmetry  $\tau_0 \otimes \tau_x$  is combined with the time-reversal symmetry ensuring the symmetry compensation in altermagnets<sup>40</sup>. The symmetry of 2-fold spin rotation ( $i\sigma_y$ ) maintains the integrity under  $SO(2)$  transformation<sup>41</sup>. Despite the spin splitting, the zero net magnetic moment is attributed to the combined symmetry that acts non-trivially on spin and cell<sup>42</sup>. The Weyl crossings between bands of the same spin but different sublattices undergo a topological transition to trivial bands upon increasing the mag-

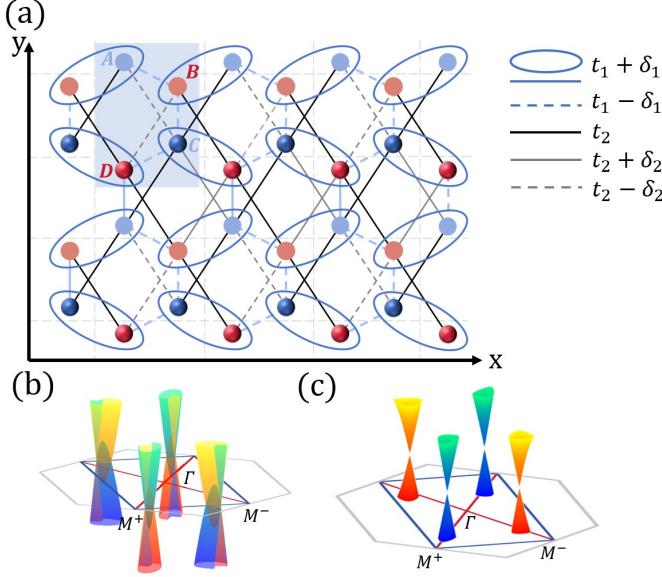


**Figure 1.** (a) Schematic of the honeycomb-lattice model for altermagnetism in group  $p6m$ . The model has four sublattices at each lattice point with red and blue dots denoting anti-aligned moments. The blue dashed lines represent the nearest-neighbor (NN) hopping strengths  $t_1 - \delta_1$ , and ellipses accompanied with blue lines are hopping terms with negative signs  $t_1 + \delta_1$ . The crystalline environment generates anisotropic second-nearest-neighbor hopping (black solid and dashed lines)  $t_2$  and  $\delta_2$ . (b) Dirac crossings with spin-up and spin-down bands develop on the BZ edges. (c) Weyl points between bands of the same spin are shown in red and blue, respectively. The massless crossings along the high-symmetry directions  $\Gamma - M$  annihilate each other into quadratic crossings with bands of opposite mirror  $M_x$  eigenvalues  $\pm 1$ .

nitude of the magnetization in altermagnets<sup>43,44</sup>. Acting as monopoles or anti-monopoles of Berry curvature, the gapped Weyl crossings enable the valley-dependent Hall effect, chiral magnetic effects, and other exotic transport phenomena<sup>45</sup>.

### Dimerized Model

We consider four distinct sublattices related by six-fold rotation as shown in fig. 1, where the cell-periodic Hamiltonian is given by

$$\begin{aligned}
 H_0(\mathbf{k}) = & \tau_0 \otimes 2t_1 [\cos(k_1) \cos(k_2) \tau_x + \cos(k_1) \sin(k_2) \tau_y] \\
 & - \tau_z \otimes 2\delta_1 [\sin(k_1) \sin(k_2) \tau_x - \sin(k_1) \cos(k_2) \tau_y] \\
 & + \tau_x \otimes t_1 [\cos(2k_2) \tau_x - \sin(2k_2) \tau_y] \\
 & - \tau_y \otimes \delta_1 [\sin(2k_2) \tau_x + \cos(2k_2) \tau_y],
 \end{aligned} \tag{1}$$

where  $\mathbf{k}_1 = \frac{\sqrt{3}}{2} \mathbf{k}_x$ ,  $\mathbf{k}_2 = \frac{1}{2} \mathbf{k}_y$ , and  $\tau_i$  are Pauli matrices acting on the wallpaper group symmetric model. When  $\delta_1 = 0$ , the

model reduces to a pristine graphene with a bulk energy gap closing along the boundary of Brillouin zone, exhibiting topologically protected linear crossing around the high-symmetry point  $(\pm \frac{\pi}{\sqrt{3}}, 0)$  shown in fig 1. (b).

We define the homeomorphism  $R^1 \cup \infty \rightarrow S^1$  with a diameter of  $\sqrt{5}$ , where the parameter of vertical axis is  $v = \frac{\delta_1}{t_1}$ . And the critical values for  $v$  are  $0, \pm \frac{\sqrt{5}}{5}, \pm \sqrt{5}$  and  $\infty$ . When  $\delta_1 = 0$ , the energy spectrum  $E = \pm t_1 \sqrt{\Lambda(\mathbf{k}) \pm 2\sqrt{\lambda(\mathbf{k})}}$ .

$$\begin{aligned}
 \Lambda(\mathbf{k}) &= 1 + 4\cos^2(k_1) + v^2 [1 + 4\sin^2(k_1)], \\
 \lambda(\mathbf{k}) &= [\cos^2(3k_2) + v^2 \sin^2(3k_2)] [4\cos^2(k_1) + 4v^2 \sin^2(k_1)] \\
 &+ v^2.
 \end{aligned} \tag{2}$$

The emergence of Dirac cones  $(\pm \frac{1}{\sqrt{3}} \arccos \frac{v^2+3}{2v^2-2}, \frac{\pi}{3})$  at the BZ corners transforms the system back to the semi-metallic phase with the gap size  $2\sqrt{1 + 5v^2 - 2v\sqrt{5}}$ . Based on spinless electrons, the Hamiltonian can be decomposed via a  $2 \times 2$  block matrix  $h_0(\mathbf{k})$  defined as

$$t_1 \begin{bmatrix} (1-v)e^{ia_1} + (1+v)e^{-ia_2} & (1+v)e^{2ik_2} \\ (1-v)e^{-2ik_2} & (1-v)e^{-ia_2} + (1+v)e^{ia_1} \end{bmatrix}, \tag{3}$$

where  $\mathbf{a}_1 = \mathbf{k}_1 - \mathbf{k}_2$  and  $\mathbf{a}_2 = \mathbf{k}_1 + \mathbf{k}_2$ . Fixing  $k_2 = 0$ , the  $h_0(\mathbf{k}_1)$  is diagonalized into  $h_0^\chi(\mathbf{k}_1) = e^{-ik_1} + 1 + \chi \sqrt{v^2(e^{-ik_1} - 1)^2 - v^2 + 1}$  through the chiral operator  $\chi$ . We derive the winding number as a topological invariant protected by chiral symmetry  $\chi = \tau_0 \otimes \tau_z$ .

$$w^\chi = \frac{1}{2\pi i} \int dk_1 \frac{d}{dk_1} \log h_0^\chi(\mathbf{k}_1), \tag{4}$$

where the topological phase transition is characterized by the sign function  $sgn(v)$ . Exhibiting a bipartite nature, the spectrum of nanoribbons has zigzag edges along the  $\mathbf{k}_1$  direction and armchair edges along the  $\mathbf{k}_2$  direction. We display the energy spectrum and density of states (DOSs) for the zigzag edge modes in fig.2. (a), while  $w_\chi = (1, 0)$  for  $v > 0$  and  $(0, 1)$  for  $v < 0$ . The zigzag ribbon presents a band of zero-energy modes that is absent in the armchair case, while the on-site potential  $\delta_m$  shifts the armchair ribbon from  $w_\chi = (0, 0)$  to  $w_\chi = (-1, 1)$  with operator  $\tau_z \otimes \tau_0$ . As shown in fig.2. (c), we analyze the wave function of bound state with  $v = 2\frac{t_1}{\hbar^2} \sqrt{1 - v^2}$ . Regarding  $\mathbf{k}_1$  as a good quantum number, the amplitudes of helical edge modes  $\psi_x = \sqrt{\frac{\hbar \delta_m}{v}} \begin{pmatrix} -i \\ 1 \end{pmatrix} e^{-\frac{\delta_m v x}{\hbar}} e^{i\frac{k_2 y}{\hbar}}$  exhibit power-law decay. Spatial distribution of the edge modes is depicted under the open boundary condition with 30 units in the perpendicular direction, which indicates the existence of propagating states along the transition interface<sup>46</sup>.

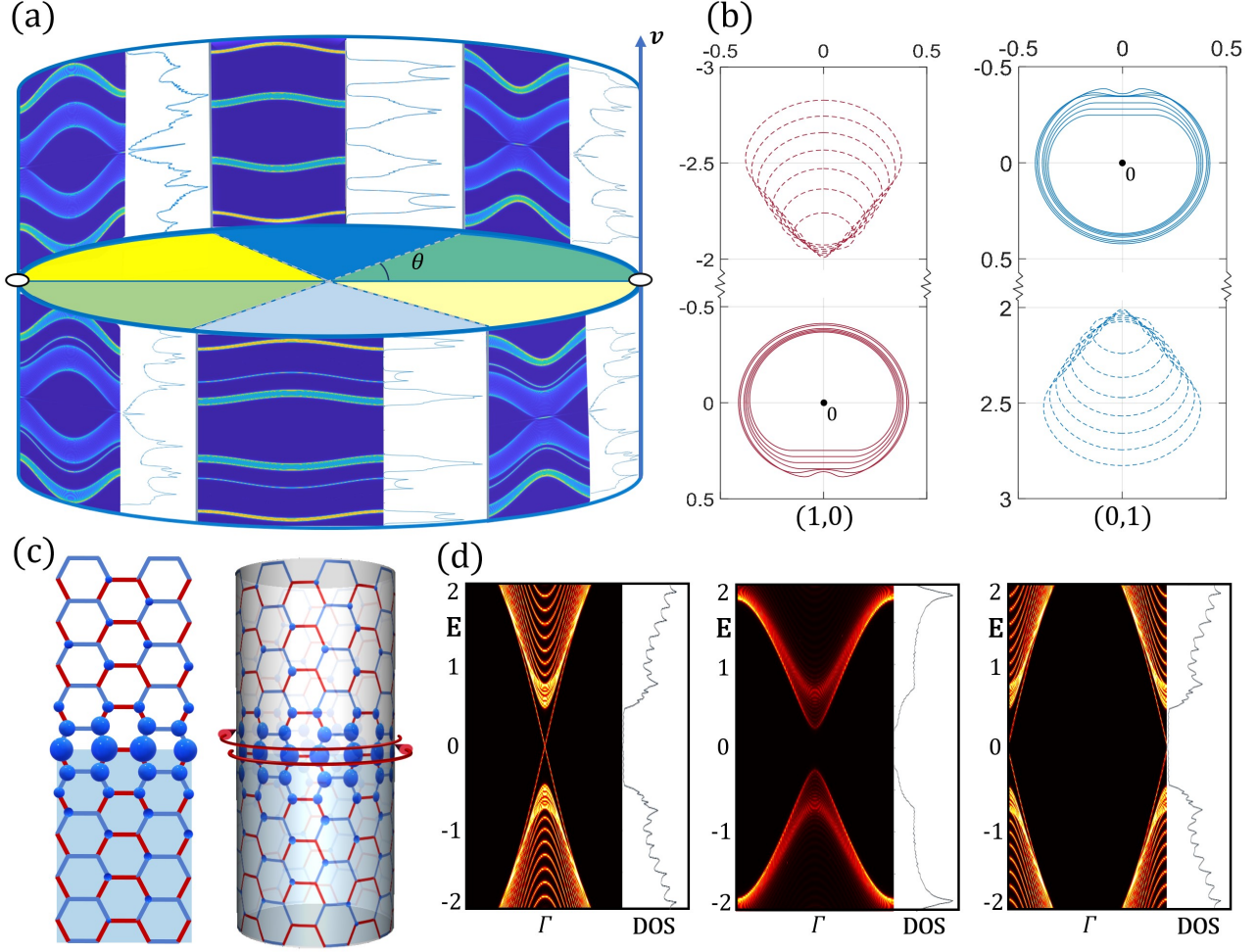


**Figure 2.** (a) Analytical demonstration of the phase diagram formed by  $\nu$  and  $\theta$ . The Dirac points merge together at the phase boundaries  $\theta = \pm \arctan \frac{\sqrt{5}}{2}$  and  $\pm(\pi - \arctan \frac{\sqrt{5}}{2})$ , where the spectral function of edge modes and DOSs are depicted for each separated phase. (b) Two pairs of winding numbers with even and odd parity. The parameters of  $\nu$  are choiced at equal intervals from -1.2 to 1.2. (c) Armchair edge modes periodic along  $k_1$  are regarded as a ribbon on a cylinde, where the amplitude of wave function are localized in the interface. (d) The energy spectrums correspond to the propagating edge modes with double degeneracy, which indicate  $(1, -1)$  for  $\nu > 0$  and  $(0, 0)$  for  $\nu < 0$ .

### Altermagnetic Quantum Hall Effect

We introduce the altermagnetism via anti-parallel magnetic moments ( $\mu = M_A - M_B = M_C - M_D$ ) from the hopping of itinerant electrons. Interacting with the localized spins among four sublattices, the itinerant electrons are sensitive to the staggered magnetization ( $\gamma = \tau_0 \otimes \tau_z$ ) via the Kondo-like coupling  $\mu\gamma$ . Based on two decoupled subspaces with well-defined spin, the  $\mu$  quantifies the interaction strength between the itinerant electrons and the collinear local moments with staggered magnetization.

The next-nearest-neighbor (NNN) hoppings for the sublattices  $A, B, C, D$  are defined as operators  $S_1 = 2\delta_2 \sin(k_1) \cos(3k_2) \tau_y \otimes \tau_z$  and  $S_2 = -2\delta_2 \cos(k_1) \sin(3k_2) \tau_y \otimes \tau_0$ , where another term related to the NNN hopping  $t_2$  is  $S_3 = 4t_2 \cos(k_1) \cos(3k_2) \tau_x \otimes \tau_0$ .

Thus, we can construct altermagnetic model from the  $\theta = \pi$  singularity of  $S^1$  in fig. 2.

$$\begin{aligned} H(\mathbf{k}) &= \sigma_0 \otimes H_1(\mathbf{k}) + \mu \sigma_z \otimes \gamma, \\ H_1(\mathbf{k}) &= H_0(\mathbf{k}) + S_1 + S_2 + S_3, \end{aligned} \quad (5)$$

where  $\sigma_i$  are Pauli matrices operating on the spin group. We calculate the energy spectrum for the  $\mu\gamma$  combined with staggered NNN hoppings as  $E^\chi = \chi\mu \pm 2\sqrt{4t_2^2 \cos^2(k_1) \cos^2(3k_2) + \delta_2^2 \sin^2(k_1 + 3\chi k_2)}$ . The quadratic energy spectrum becomes subject to the altermagnetic potentials that lifts the spin-degeneracy. As a critical point in fig. 2, the  $t_1$  term opens the altermagnetic nodal line generating the spin-polarized Dirac cones with  $\delta_1 = 0$ . We map

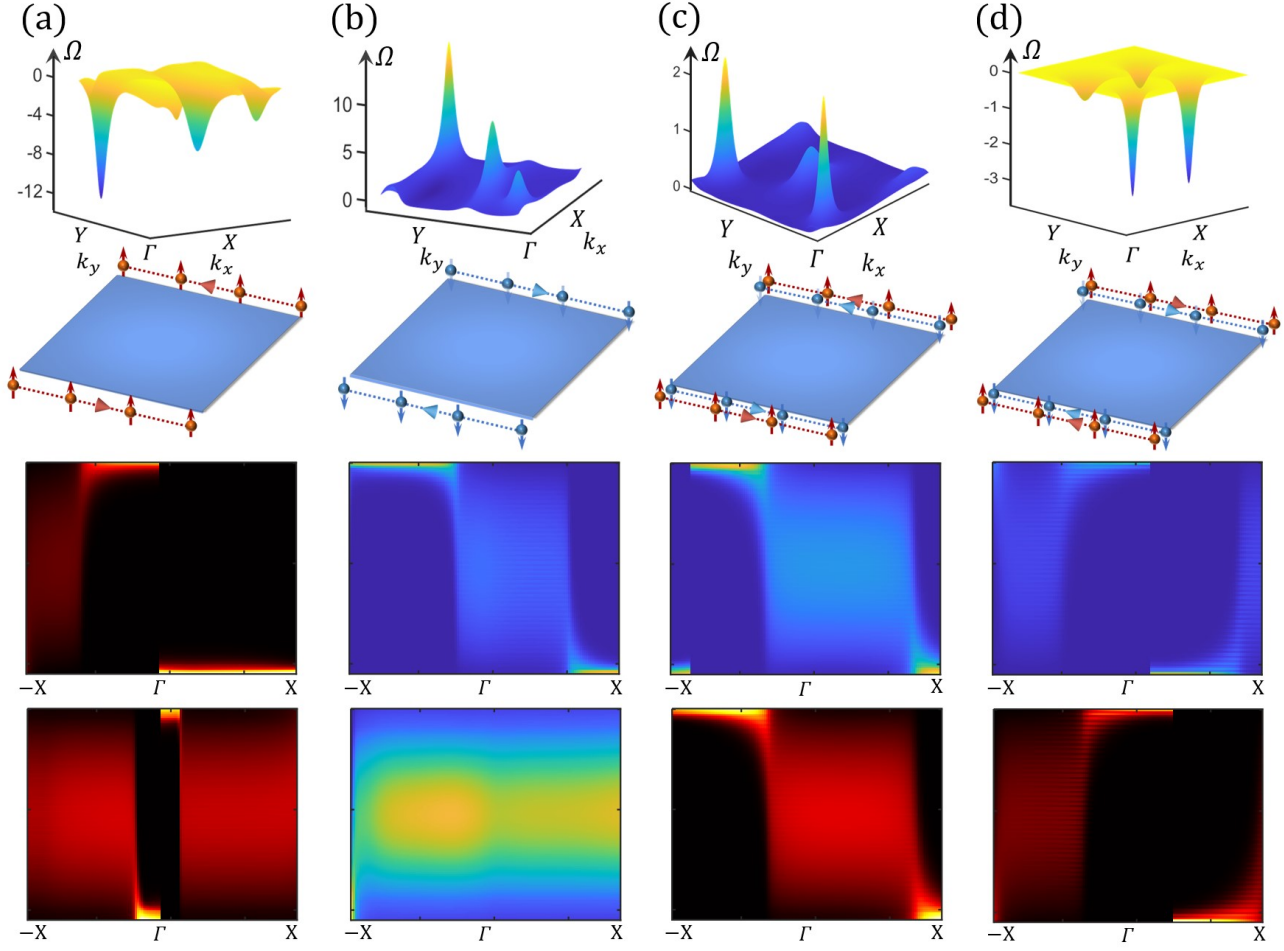


**Figure 3.** The distribution of Berry curvature and the amplitude of localized edge modes in the limit of  $\nu \rightarrow \infty$ . (a) The directions of spin-up edge currents with  $C = 1$ . We use the parameters  $t_2=0.6$ ,  $\delta_2=1.2$ ,  $|\mu|=0.6$ , and set the coefficients of mass terms as  $m_1=1$ ,  $m_2=1.3$ . (b) The directions of spin-down edge currents with  $C=-1$ . We use  $\delta_2=-1.2$  setting the same other parameters as the former. (c) The spin-polarized current with  $C=2$ . We use the parameters  $t_2=0.6$ ,  $\delta_2=1.2$ ,  $|\mu|=4$  fixing the mass term  $m_2=0.3$ . (d) The spin-polarized current with  $C = -2$ . We use  $\delta_2 = -1.2$  with the same other parameters as the former.

the effective Hamiltonian into the subspace via the operator  $P=|\Psi^\alpha(\mathbf{k})\rangle\langle\Psi^\alpha(\mathbf{k})|\oplus|\Psi^\beta(\mathbf{k})\rangle\langle\Psi^\beta(\mathbf{k})|$ .

$$\begin{aligned} H_{q^\alpha} &= \epsilon_q^\alpha \sigma_0 + v_x^\alpha q_x^\alpha \sigma_y \pm v_y^\alpha q_y^\alpha \sigma_x, \\ H_{q^\beta} &= \epsilon_q^\beta \sigma_0 + v_x^\beta q_x^\beta \sigma_y \pm v_y^\beta q_y^\beta \sigma_x, \end{aligned} \quad (6)$$

where  $\epsilon_q^\alpha = \epsilon_q^\beta = 0$  are half filled Fermi energy. The anisotropic velocities for spin-up subspace are  $v_x^\alpha$  and  $v_y^\alpha$ , where the counterparts for spin-down are represented by  $\beta$ . The presence of  $t_1$  reshapes the subspace algebraic structure via  $\xi = |\frac{R^2}{2\delta_2^2} - 1|$ ,  $R^2 = t_1^2 + \mu^2$ . We derive the anisotropic velocities in the vicinity of pair-wise crossings  $(\pm \frac{\pi}{\sqrt{3}}, \pm \frac{\pi - \arccos \sqrt{\xi}}{3})$ .

$$\begin{aligned} v_y^\alpha &= v_y^\beta = \delta_2 \sqrt{3\xi}, \\ v_x^{\alpha\beta} &= \sqrt{|9\delta_2^2 - 9R^2 + \chi 18R^2 \cos^4 \frac{\sqrt{1-\xi}}{3}|}. \end{aligned} \quad (7)$$

Without considering the SOC, the dispersion relation approaches a linear behavior, where two spin-degenerate points can form a fourfold degeneracy near the Fermi level with additional mirror symmetry protection. The bands of opposite spins hold the topologically protected 4-fold Dirac crossings on the  $MX$  line owing to the mirror operation not swapping the sublattices. The mass term  $M_k = m_1 \cos(2k_1) + m_2 \sin(2k_1) + m_3 \sin(2k_2)$  is also introduced by multiplying the general staggered hoppings with the lattice space operator  $\tau_z \otimes \tau_0$ . Thus, the topology of crossing is characterized by the Berry Phase  $\Upsilon_\pm^{\alpha(\beta)}$ .

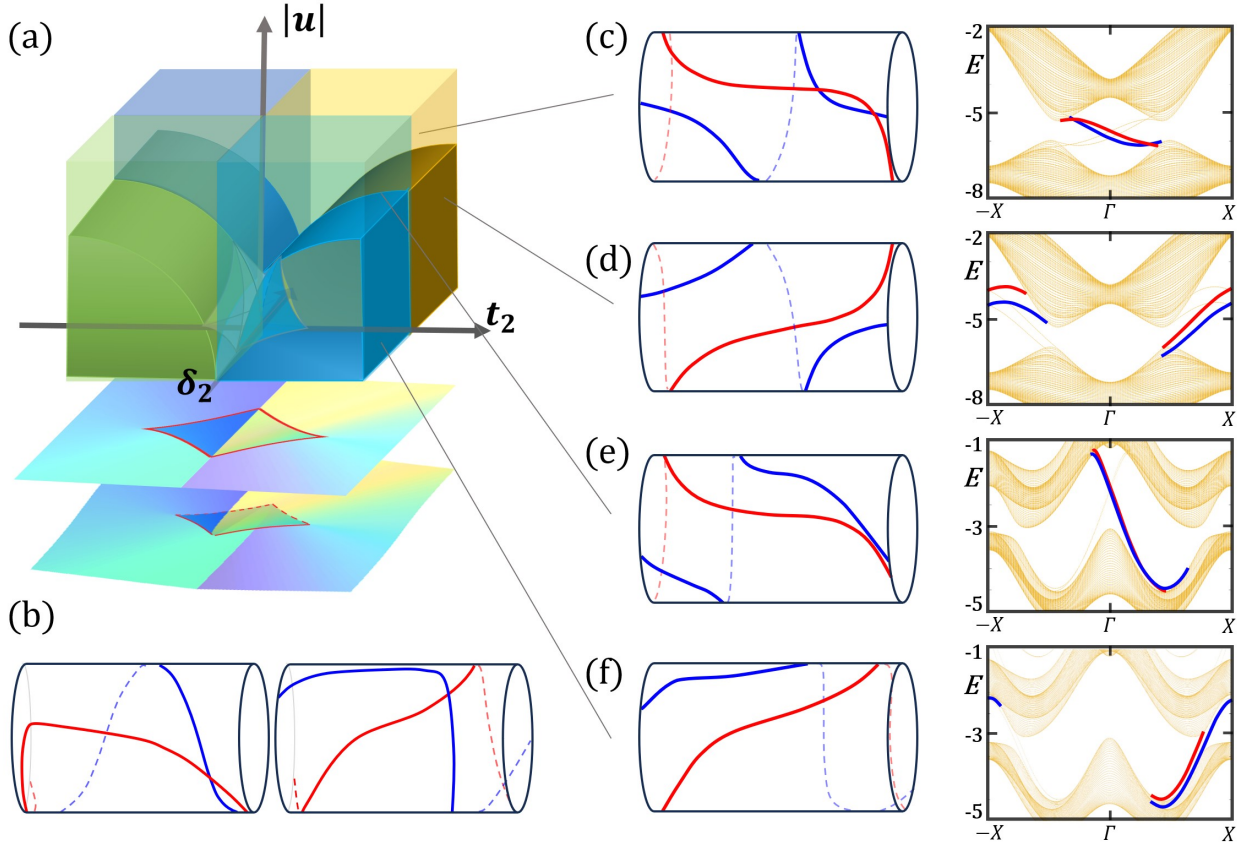


**Figure 4.** (a) The Weyl phase diagram demonstrates the formation of Weyl points, where the phase boundary is related to the singularity class when the map sends regular values to a critical values. The number of Weyl points in the vertical axis is determined by the staggered potential  $\mu$ . (b) The flows of Wannier centers for  $|C|=1$  with equivalent parameter choices as fig. 3. (c)-(f) The curved surface separates the creation of weyl points from the gapped phase with  $|\mu|=0.6$ . The red line shows the chiral propagating states for spin-up, whereas the spin-down counterpart is in blue.

$$\begin{aligned}
Y_{\pm}^{\alpha(\beta)} &= \pm \frac{1}{4\pi} \int_{BZ} \frac{\mathbf{d}_q^{\alpha(\beta)} \cdot [\partial_{q_x} \mathbf{d}_q^{\alpha(\beta)} \times \partial_{q_y} \mathbf{d}_q^{\alpha(\beta)}]}{|\mathbf{d}_q^{\alpha(\beta)}|^3}, \\
&= \pm \frac{1}{4\pi} \int_{BZ} \frac{M_k v_x v_y}{2 \sqrt{v_x q_y^2 + v_y q_x^2 + M^2}} = \pm \frac{\text{sgn}(M_k)}{2}, \quad (8)
\end{aligned}$$

where  $\mathbf{d}_q^{\alpha(\beta)} = v_y^{\alpha(\beta)} \mathbf{q}_x + v_x^{\alpha(\beta)} \mathbf{q}_y + \frac{M_k}{2} \mathbf{q}_z$ . The distribution of Berry curvature contributes to the total Hall current as  $j = \frac{\hbar}{2e} (j^\alpha + j^\beta) = \frac{e^2}{\hbar} \sum \alpha, \beta \text{sgn}(M_k)$ <sup>47</sup>. The tilted Dirac points exhibit robust stability protected by time-reversal and spin-inversion symmetries, while the mirror symmetry acts as a stabilizing operator for Dirac points, remaining degenerate along the mirror-symmetric lines.

### Weyl Phase Diagram

We depict the relevant Wannier center flows by non-Abelian Berry phase in fig.4, corresponding to the integration of Berry curvature with fully decoupled spin

subspaces<sup>48,49</sup>. The mirror symmetry permits us to adopt the following ansatz for the wave functions  $\Psi = (\psi_{1A}, \psi_{1B}, \psi_{1C}, \psi_{1D}, \dots, \psi_{nA}, \psi_{nB}, \psi_{nC}, \psi_{nD})^\dagger$ . Thus, the retarded and advanced Green's functions are  $G^R(r, r') = \sum_{k,n} \frac{\Psi_{k,n}^\dagger(r') \Psi_{k,n}(r)}{E + i\eta - H}$ ,  $G^A(r, r') = [G^R(r, r')]^\dagger$ , where  $\eta$  is a positive infinitesimal,  $r$  and  $r'$  represent excitation and response respectively. For the purpose of calculating transport properties, we introduce the spectral representation of the Green's function which can be written as  $A = \sum_{k,n} \Psi_{k,n}(r) \Psi_{k,n}^\dagger(r') \frac{2\eta}{(E-H)^2 + \eta^2}$ , and the DOS can also be defined as  $\rho(\epsilon) = \sum_{k,n} \Psi_{k,n} \Psi_{k,n}^\dagger \delta(E - H) = \frac{\hbar \text{Tr}(A)}{2\pi}$ .

The Weyl phase diagram is formed by  $t_2$  and  $\delta_2$  in the configurational space fixing  $t_1=0$  and  $\delta_1=1$ . The Wilson loop approach describes the evolution of Wannier function center based on the  $U(2N)$  Berry connection  $A^{\alpha\beta} = \langle \Psi^\alpha(\mathbf{k}) | \Psi^\beta(\mathbf{k} + \delta_k) \rangle$ . We project the  $H_0(\mathbf{k})$  into the Bloch occupied states via the position operator  $\sum_k \sum_{\alpha, \beta=1}^{N_F} A^{\alpha\beta} |\Psi^\beta(\mathbf{k} + \delta_k)\rangle \langle \Psi^\alpha(\mathbf{k})|$ . Typical phases are illustrated in fig.4, which are modified by varying the staggered magnetization as the control parameter.

We bridge a connection between the mappings of manifolds  $M^2 \rightarrow R^2$ , where  $R^2$  is two-dimensional Euclidean space. The emergence of pairwise Weyl points creates a cusp point from the map self-intersection.

The spin degeneracy of the edge modes is lifted allowing for unique chiral propagating states under the  $Z_2$  topological classification<sup>50</sup>. We theoretically calculate the quantum Hall effects via the controlled fabrication of the valley degree of freedom in altermagnetic band structure in fig.4. The formation of Weyl points enables nontrivial topology for spin splitting band structure, acting as monopoles or anti-monopoles of Berry curvature determined by their chirality. We depict the zigzag edges of altermagnetic ribbon, where the magnetic moments on adjacent sites are antiparallel. Induced by the antiparallel orientation of magnetic moments, the gap opening at the Weyl points illustrates chiral transport responses rather than helical spin textures<sup>51,52</sup>. We suggest the injection of high-energy photons can induce non-trivial topological states in our altermagnetic model, where the radiative recombination of spin-polarized carriers exhibits a net circular polarization<sup>53</sup>. These states can also be realized in non-Hermitian systems through the modulation of gain and loss, both of which are guided by mirror symmetry and  $PT$  symmetry<sup>54</sup>.

## Possible experimental realizations

Allowing for high Néel temperature, altermagnetism represents a frontier in the study of magnetic materials<sup>55–58</sup>, while the application of an out-of-plane electric field can modulate the magnetic interactions to more complex magnetic orderings<sup>59,60</sup>. The unique interplay of lattice symmetries suggest  $\text{MnP}(\text{S,Se})_3$  might be functionalized into a strong altermagnet from a 2D antiferromagnet<sup>61</sup>. The time-reversal symmetry breaking in monolayer FeSe is also not simply a manifestation of ferromagnetism but rather an indication of altermagnetism<sup>62,63</sup>. Combined with the Kerr effect, the polarized photons interacting with the staggered magnetic moments can regulate topological responses in advanced optoelectronic devices<sup>64,65</sup>.

Ultracold atoms in optical lattices offer a highly controllable platform for studying altermagnetic topology<sup>66</sup>. Based on broken time-reversal symmetry, our model can be realized in  $C_{6v}$ -symmetrical hexagonal lattices by breaking mirror symmetry, providing a versatile platform for the study of topological phenomena in elasticity. By tuning the lattice parameters, we can engineer our model into different topological regimes via artificial mechanical lattices, allowing for the observation of the robust transport for chiral edge modes. In ultracold atomic gases, the realization of synthetic magnetic fields allow us to engineer various topological phases and observe valley-dependent Hall effects in a controllable manner<sup>67,68</sup>.

Topoelectrical circuits hold promise to manipulate the valley polarization through topological boundary resonances<sup>69,70</sup>. We consider a honeycomb lattice structure with engineered parameters to achieve bond dimerization and onsite potentials.

As one of the potential networks for altermagnetic application, the tunability of edge states exists even in the absence of SOC due to the intrinsic topology of the Weyl circuits. The direction of propagation of the electromagnetic waves, representing the valley-polarized modes, depends on the handedness of the orbital angular momentum of the excitation source<sup>71–73</sup>. Topoelectrical circuits exploit the inherent degeneracy to engineer robust states that are immune to backscattering and disorder, enabling the realization of the valleytronic devices and the application of topological quantum computing<sup>74,75</sup>.

## Acknowledgements

We thank Zi-Jian Xiong for helpful discussions. This project is supported by NKRDPC-2022YFA1402802, NSFC-92165204, NSFC-12494590, Leading Talent Program of Guangdong Special Projects (201626003), Guangdong Provincial Key Laboratory of Magnetoelectric Physics and Devices (No. 2022B1212010008), Research Center for Magnetoelectric Physics of Guangdong Province(2024B0303390001), and Guangdong Provincial Quantum Science Strategic Initiative (GDZX2401010).

## References

1. Zhu, Y.-P. *et al.* Observation of plaid-like spin splitting in a noncoplanar antiferromagnet. *Nature* **626**, 523 (2024).
2. Hayami, S., Yanagi, Y. & Kusunose, H. Momentum-dependent spin splitting by collinear antiferromagnetic ordering. *J. Phys. Soc. Jpn.* **88**, 123702 (2019).
3. Yuan, L.-D., Wang, Z., Luo, J.-W., Rashba, E. I. & Zunger, A. Giant momentum-dependent spin splitting in centrosymmetric low- $z$  antiferromagnets. *Phys. Rev. B* **102**, 014422 (2020).
4. Yuan, L.-D., Wang, Z., Luo, J.-W. & Zunger, A. Prediction of low- $z$  collinear and noncollinear antiferromagnetic compounds having momentum-dependent spin splitting even without spin-orbit coupling. *Phys. Rev. Mater.* **5**, 014409 (2021).
5. Han, L. *et al.* Electrical 180° switching of néel vector in spin-splitting antiferromagnet. *Sci. Adv.* **10**, eadn0479 (2024).
6. Šmejkal, L., Sinova, J. & Jungwirth, T. Emerging research landscape of altermagnetism. *Phys. Rev. X* **12**, 040501 (2022).
7. Chiu, C. K., Chan, Y. H. & Schnyder, A. P. Quantized berry phase and surface states under reflection symmetry or space-time inversion symmetry. *arXiv* 1810.04094 (2018).
8. Bhowal, S. & Spaldin, N. A. Ferroically ordered magnetic octupoles in  $d$ -wave altermagnets. *Phys. Rev. X* **14**, 011019 (2024).

9. Lin, Z. *et al.* Observation of giant spin splitting and d-wave spin texture in room temperature altermagnet  $\text{RuO}_2$ . *arXiv* 2402.04995 (2024).
10. Ding, J. *et al.* Large band-splitting in g-wave type altermagnet  $\text{CrSb}$ . *Phys. Rev. Lett.* **133** (2024).
11. Bühler, A. *et al.* Majorana modes and p-wave superfluids for fermionic atoms in optical lattices. *Nat. Commun.* **5**, 4504 (2014).
12. Zhang, S.-B., Hu, L.-H. & Neupert, T. Finite-momentum cooper pairing in proximitized altermagnets. *Nat. Commun.* **15**, 1801 (2024).
13. Zhu, D., Zhuang, Z.-Y., Wu, Z. & Yan, Z. Topological superconductivity in two-dimensional altermagnetic metals. *Phys. Rev. B* **108**, 184505 (2023).
14. Castro Neto, A. H., Guinea, F., Peres, N. M. R., Novoselov, K. S. & Geim, A. K. The electronic properties of graphene. *Rev. Mod. Phys.* **81**, 109–162, DOI: [10.1103/RevModPhys.81.109](https://doi.org/10.1103/RevModPhys.81.109) (2009).
15. Šmejkal, L., Sinova, J. & Jungwirth, T. Beyond conventional ferromagnetism and antiferromagnetism: A phase with nonrelativistic spin and crystal rotation symmetry. *Phys. Rev. X* **12**, 031042 (2022).
16. Zeng, S. & Zhao, Y.-J. Description of two-dimensional altermagnetism: Categorization using spin group theory. *Phys. Rev. B* **110**, 2469–9969 (2024).
17. Liu, P., Li, J., Han, J., Wan, X. & Liu, Q. Spin-group symmetry in magnetic materials with negligible spin-orbit coupling. *Phys. Rev. X* **12**, 021016 (2022).
18. Chen, X. *et al.* Enumeration and representation theory of spin space groups. *Phys. Rev. X* **14**, 031038 (2024).
19. Geim, A. K. Graphene: Status and prospects. *Science* **324**, 1530–1534 (2009).
20. Li, C. *et al.* Topological weyl altermagnetism in  $\text{CrSb}$ . *arXiv* 2405.14777 (2024).
21. Liu, S. *et al.* Ferromagnetic weyl fermions in two-dimensional layered electride  $\text{gd}_2\text{C}$ . *Phys. Rev. Lett.* **125**, 187203 (2020).
22. Parshukov, K., Wiedmann, R. & Schnyder, A. P. Topological responses from gapped weyl points in 2d altermagnets. *arXiv* 2403.09520 (2024).
23. Zeng, M. *et al.* Observation of spin splitting in room-temperature metallic antiferromagnet  $\text{CrSb}$ . *Adv. Sci.* **11**, 2406529 (2024).
24. Sheoran, S. & Bhattacharya, S. Nonrelativistic spin splittings and altermagnetism in twisted bilayers of centrosymmetric antiferromagnets. *arXiv* 2310.19395 (2024).
25. Yu, Y., Suh, H.-G., Roig, M. & Agterberg, D. F. Altermagnetism from coincident van hove singularities: application to  $\kappa\text{-Cl}$ . *arXiv* 2402.05180 (2024).
26. Fang, Y., Cano, J. & Ghorashi, S. A. A. Quantum geometry induced nonlinear transport in altermagnets. *Phys. Rev. Lett.* **133**, 106701 (2024).
27. Ezawa, M. Detecting the néel vector of altermagnets in heterostructures with a topological insulator and a crystalline valley-edge insulator. *Phys. Rev. B* **109**, 245306 (2024).
28. Turek, I. Altermagnetism and magnetic groups with pseudoscalar electron spin. *Phys. Rev. B* **106**, 094432 (2022).
29. Jiang, Y. *et al.* Enumeration of spin-space groups: Toward a complete description of symmetries of magnetic orders. *Phys. Rev. X* **14**, 031039 (2024).
30. Brinkman, W. F., Elliott, R. J. & Peierls, R. E. Theory of spin-space groups. *Proc. Royal Soc. London. Ser. A. Math. Phys. Sci.* **294**, 343–358 (1966).
31. Fedchenko, O. *et al.* Observation of time-reversal symmetry breaking in the band structure of altermagnetic  $\text{RuO}_2$ . *Sci. Adv.* **10**, eadj4883 (2024).
32. Antonenko, D. S., Fernandes, R. M. & Venderbos, J. W. F. Mirror chern bands and weyl nodal loops in altermagnets. *arXiv* 2402.10201 (2024).
33. Gao, Z.-F. *et al.* Ai-accelerated discovery of altermagnetic materials. *arXiv* 2311.04418 (2024).
34. Bernardini, F., Fiebig, M. & Cano, A. Ruddlesden-popper and perovskite phases as a material platform for altermagnetism. *arXiv* 2401.12910 (2024).
35. Miró, P., Audiffred, M. & Heine, T. An atlas of two-dimensional materials. *Chem. Soc. Rev.* **43**, 6537–6554 (2014).
36. Lee, Y.-L. Magnetic impurities in an altermagnetic metal. *arXiv* 2312.15733 (2023).
37. Ma, H. *et al.* Multifunctional antiferromagnetic materials with giant piezomagnetism and noncollinear spin current. *Nat. Commun.* **12**, 2846 (2021).
38. Šmejkal, L., Sinova, J. & Jungwirth, T. Beyond conventional ferromagnetism and antiferromagnetism: A phase with nonrelativistic spin and crystal rotation symmetry. *Phys. Rev. X* **12**, 031042 (2022).
39. Fu, L. & Kane, C. L. Topological insulators with inversion symmetry. *Phys. Rev. B* **76**, 045302 (2007).
40. Slager, R.-J., Mesaros, A., Juričić, V. & Zaanen, J. Interplay between electronic topology and crystal symmetry: Dislocation-line modes in topological band insulators. *Phys. Rev. B* **90**, 241403 (2014).
41. Teo, J. C. & Hughes, T. L. Topological defects in symmetry-protected topological phases. *Annu. Rev. Condens. Matter Phys.* **8**, 211–237 (2017).
42. Chiu, C.-K., Teo, J. C. Y., Schnyder, A. P. & Ryu, S. Classification of topological quantum matter with symmetries. *Rev. Mod. Phys.* **88**, 035005 (2016).

43. Nag, J. *et al.* Gdalsi: An antiferromagnetic topological weyl semimetal with non-relativistic spin splitting. *arXiv* 2312.11980 (2024).
44. Soto-Garrido, R., Muñoz, E. & Juričić, V. Dislocation defect as a bulk probe of monopole charge of multi-weyl semimetals. *Phys. Rev. Res.* **2**, 012043 (2020).
45. Chen, X., Wang, D., Li, L. & Sanyal, B. Giant spin-splitting and tunable spin-momentum locked transport in room temperature collinear antiferromagnetic semimetallic cro monolayer. *Appl. Phys. Lett.* **123**, 022402 (2023).
46. van Miert, G. & Ortix, C. Dislocation charges reveal two-dimensional topological crystalline invariants. *Phys. Rev. B* **97**, 201111 (2018).
47. Qi, X.-L., Wu, Y.-S. & Zhang, S.-C. Topological quantization of the spin hall effect in two-dimensional paramagnetic semiconductors. *Phys. Rev. B* **74**, 085308 (2006).
48. Yamamoto, A. Berry phase in lattice qcd. *Phys. Rev. Lett.* **117**, 052001 (2016).
49. Xiao, D., Chang, M.-C. & Niu, Q. Berry phase effects on electronic properties. *Rev. Mod. Phys.* **82**, 1959–2007 (2010).
50. Rhim, J.-W., Behrends, J. & Bardarson, J. H. Bulk-boundary correspondence from the intercellular zak phase. *Phys. Rev. B* **95**, 035421 (2017).
51. Šmejkal, L., González-Hernández, R., Jungwirth, T. & Sinova, J. Crystal time-reversal symmetry breaking and spontaneous hall effect in collinear antiferromagnets. *Sci. Adv.* **6**, eaaz8809 (2020).
52. Hoyer, R., Jaeschke-Ubiergo, R., Ahn, K.-H., Šmejkal, L. & Mook, A. Spontaneous crystal thermal hall effect in insulating altermagnets. *arXiv* 2405.05090 (2024).
53. Wang, J., Chen, X., Zhu, B.-F. & Zhang, S.-C. Topological  $p$ - $n$  junction. *Phys. Rev. B* **85**, 235131 (2012).
54. Young, A. F. & Kim, P. Quantum interference and klein tunnelling in graphene heterojunctions. *Nat. Phys.* **5**, 222–226 (2009).
55. Mazin, I. I., Koepernik, K., Johannes, M. D., González-Hernández, R. & Šmejkal, L. Prediction of unconventional magnetism in doped  $fesb_2$ . *Proc. Natl. Acad. Sci.* **118**, e2108924118 (2021).
56. Guo, P.-J., Gu, Y., Gao, Z.-F. & Lu, Z.-Y. Altermagnetic ferroelectric life2f6 and spin-triplet excitonic insulator phase. *arXiv* 2312.13911 (2023).
57. Milivojević, M., Orozović, M., Picozzi, S., Gmitra, M. & Stavrić, S. Interplay of altermagnetism and weak ferromagnetism in two-dimensional ruf4. *2D Mater.* **11**, 035025 (2024).
58. Mazin, I. I. Altermagnetism in mnte: Origin, predicted manifestations, and routes to detwinning. *Phys. Rev. B* **107**, L100418 (2023).
59. Hariki, A. *et al.* X-ray magnetic circular dichroism in altermagnetic  $\alpha$ -mnte. *Phys. Rev. Lett.* **132**, 176701 (2024).
60. Lee, S. *et al.* Broken kramers degeneracy in altermagnetic mnte. *Phys. Rev. Lett.* **132**, 036702 (2024).
61. Mazin, I., González-Hernández, R. & Šmejkal, L. Induced monolayer altermagnetism in  $mnp(s,se)_3$  and  $fese$ . *arXiv* 2309.02355 (2023).
62. Wei, C.-C. *et al.*  $La_2O_3Mn_2Se_2$ : a correlated insulating layered d-wave altermagnet. *arXiv* 2410.14542 (2024).
63. Ezawa, M. Third-order and fifth-order nonlinear spin-current generation in  $g$ -wave and  $i$ -wave altermagnets and perfect spin-current diode based on  $f$ -wave magnets. *arXiv* 2411.16036 (2024).
64. Eschbach, M. *et al.* Realization of a vertical topological  $p$ - $n$  junction in epitaxial  $sb_2te_3/bi_2te_3$  heterostructures. *Nat. Commun.* **6**, 8816 (2015).
65. Ilan, R., de Juan, F. & Moore, J. E. Spin-based mach-zehnder interferometry in topological insulator  $p$ - $n$  junctions. *Phys. Rev. Lett.* **115**, 096802 (2015).
66. Das, P., Leeb, V., Knolle, J. & Knap, M. Realizing altermagnetism in fermi-hubbard models with ultracold atoms. *Phys. Rev. Lett.* **132**, 263402 (2024).
67. Zhai, X. & Blanter, Y. M. Topological valley transport of gapped dirac magnons in bilayer ferromagnetic insulators. *Phys. Rev. B* **102**, 075407 (2020).
68. Xiao, D., Yao, W. & Niu, Q. Valley-contrasting physics in graphene: Magnetic moment and topological transport. *Phys. Rev. Lett.* **99**, 236809 (2007).
69. Huang, Y. & Chen, X. Quantum circuit complexity of one-dimensional topological phases. *Phys. Rev. B* **91**, 195143 (2015).
70. Ningyuan, J., Owens, C., Sommer, A., Schuster, D. & Simon, J. Time- and site-resolved dynamics in a topological circuit. *Phys. Rev. X* **5**, 021031 (2015).
71. Lee, C. H. *et al.* Topoelectrical circuits. *Commun. Phys.* **1**, 39 (2018).
72. Paler, A., Polian, I., Nemoto, K. & Devitt, S. J. Fault-tolerant, high-level quantum circuits: form, compilation and description. *Quantum Sci. Technol.* **2**, 025003 (2017).
73. Paler, A., Fowler, A. G. & Wille, R. Synthesis of arbitrary quantum circuits to topological assembly: Systematic, online and compact. *Sci. Reports* **7**, 10414 (2017).
74. Paler, A., Devitt, S. J., Nemoto, K. & Polian, I. Mapping of topological quantum circuits to physical hardware. *Sci. Reports* **4**, 4657 (2014).
75. Roushan, P. *et al.* Observation of topological transitions in interacting quantum circuits. *Nature* **515**, 241 (2014).